

# We are IntechOpen, the world's leading publisher of Open Access books Built by scientists, for scientists

6,900

Open access books available

186,000

International authors and editors

200M

Downloads

Our authors are among the

154

Countries delivered to

TOP 1%

most cited scientists

12.2%

Contributors from top 500 universities



WEB OF SCIENCE™

Selection of our books indexed in the Book Citation Index  
in Web of Science™ Core Collection (BKCI)

Interested in publishing with us?  
Contact [book.department@intechopen.com](mailto:book.department@intechopen.com)

Numbers displayed above are based on latest data collected.  
For more information visit [www.intechopen.com](http://www.intechopen.com)



---

# Petrographical and Mineralogical Applications of Raman Mapping

---

Frédéric Foucher, Guillaume Guimbretière,  
Nicolas Bost and Frances Westall

Additional information is available at the end of the chapter

<http://dx.doi.org/10.5772/65112>

---

## Abstract

Raman spectroscopy has undergone rapid development over the last few decades. The ability to acquire a spectrum in only a few tens of milliseconds allows use of Raman mapping as a routine technique. However, with respect to classical single spectrum measurement, this technique is not still as widely used as it could be, in particular for mineralogy and petrography. Here, we explain the advantages of Raman mapping for obtaining additional information compared to single spot analyses. The principle and the limits of the technique are first explained in 2D and 3D. Data processing techniques are then described using different types of rocks and minerals to demonstrate the utility of Raman mapping for obtaining information about the general composition, identification of small phases, as well as for distinguishing minerals that are spectrally very close. More “exotic” uses of the collected signal are also described. Finally, a gallery of images from representative samples is used to illustrate the discussion.

**Keywords:** Raman mapping, petrography, mineralogy

---

## 1. Introduction

The Raman effect was described for the first time by Chandrasekhara Venkata Rāman in 1928. Raman spectroscopy is a very powerful technique allowing study of atomic bonds and identification of crystalline structures. Contrary to energy dispersive X-ray spectroscopy (EDX) or the electron microprobe, for example, Raman does not give the elemental composition of the sample but can identify organic molecules and mineralogical phases. No sample preparation is required, and the analysis can be made on the sample surface or below the surface, depending

on sample transparency. For technical reasons, the technique began to be widely used only at the beginning of the 1980s with the generalisation of lasers. At the end of the 1990s, Raman spectroscopy underwent a second phase of development with the introduction of Charge Couple Device (CCD) technology, which has widely improved the sensitivity of spectrometers. These technical revolutions allow acquisition of a Raman spectrum in only few milliseconds. This strong decrease in the acquisition time permitted development of new applications, in particular Raman mapping. This technique consists of scanning the sample with the laser while acquiring spectra so that spatial distribution can be added to structural information.

Here, we present the principle of the technique and the basis of the associated data processing followed by an overview of the information that can be extracted from Raman mapping to improve mineralogical and petrological analyses. In particular, we discuss how it can be used to study the general composition of rocks, to detect and identify small phases, or to differentiate minerals whose spectra are very close. More exotic uses of the collected signal are also presented, e.g., detection of particular phases using luminescence. Finally, we illustrate the discussion using a number of different types of rocks and minerals.

## 2. Principle and instrumentation

### 2.1. Raman spectroscopy

The Raman effect is due to inelastic interaction between photons and atomic bonds. In this process, the scattered photons lose or gain energy with respect to the incident photons by vibrating or stabilising the atomic bonds of the sample. This effect leads to a shift in energy called the Stokes shift if the photons lose energy and the Anti-Stokes shift if the photons gain energy. At room conditions, the Stokes part of the Raman signal is generally stronger and is, therefore, generally used in Raman analysis. Due to the quantification of the energy and to the activated vibrational modes, photons are only scattered for particular energies and thus for particular wavelengths. Therefore, Raman scattering of a monochromatic light by molecular entities or an ordered solid will give spectra consisting of sharp spectral lines. Most systems today use a CCD camera interfaced with the spectrometer. The collected signal is then represented in a graph showing the number of photons versus wavenumber, i.e., the shift in  $\text{cm}^{-1}$  with respect to the incident beam, the laser wavelength corresponding then to  $0 \text{ cm}^{-1}$ . The spectral resolution is limited by the CCD camera resolution and by the grating used to diffract the light. It also depends on the laser wavelength. Since the Raman effect is sensitive to atomic bonds, a Raman spectrum is associated with only one compound and its intensity is proportional to its concentration. Polymorphic minerals (similar compositions but different crystal-line structures) will thus have different spectra. For example, anatase, rutile and brookite have different Raman spectra despite their similar composition ( $\text{TiO}_2$ ). It is important to note that different parameters may influence the Raman signal, such as instrumental setup, structural defects, traces elements, internal stresses or temperature [1–3] (**Figure 1**). Although these parameters may sometimes complicate interpretation, some of them can also be used to measure particular properties, for example, the shift related to internal stresses [4].

Finally, the Raman effect is relatively complex to model, and the identification of a compound is generally made by comparison with reference spectra found in the literature or in databases. More information about the Raman effect can be found in this book or others [5–7].

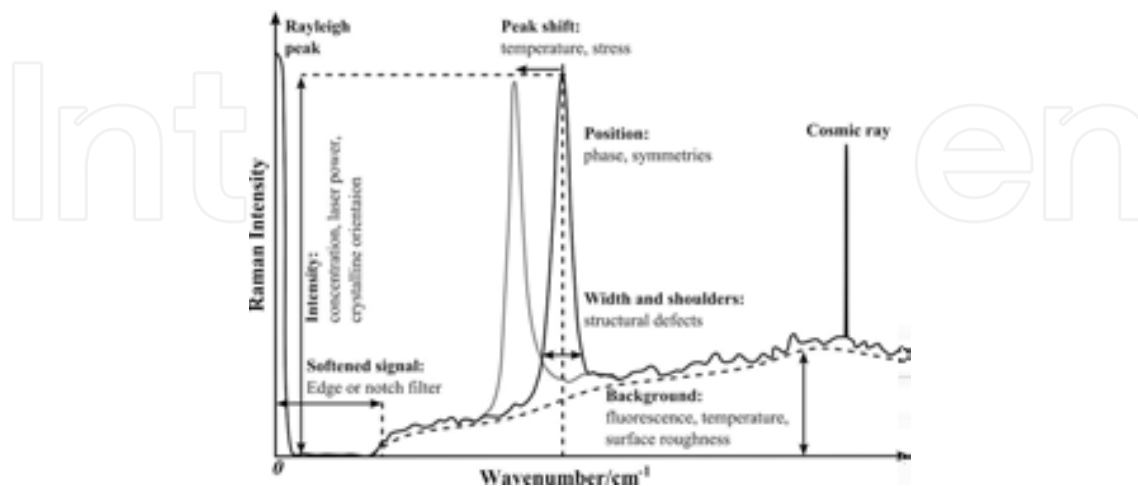


**Figure 1.** Origins of the parameters and modifications of the Raman spectrum [1].

## 2.2. Instrumentation

Raman mapping consists of scanning a sample with the laser beam while acquiring spectra. For the study example, we present here, a WITec Alpha500 RA Raman spectrometer was used. Other systems from Renishaw, Horiba Jobin Yvon, Thermo Fisher or Bruker, for example, may use slightly different methods for mapping, but the general principle of scanning remains the same. The general discussion of this chapter can thus be applied to any other system.

This study was made using a CW green Nd:YAG frequency doubled laser with a wavelength of  $\lambda = 532$  nm. The laser beam is focused on the sample using optical microscope objectives and optical observations of the analysed area are made with a camera. The spectral resolution of the spectrometer is of 1 and 3  $\text{cm}^{-1}$  using 1800 and 600 g/mm gratings, respectively. Surface scanning is made by moving the sample below the objective along successive lines using motorised and/or piezoelectric scan tables. The instrument used is equipped with two positioning systems: (1) a small-scale system working with piezoelectric ceramics that can analyse an area of  $200 \times 200 \mu\text{m}$  in the horizontal plan and  $20 \mu\text{m}$  in the vertical direction and (2) a large-scale motorised system that can move the sample over a distance of  $15 \times 10$  cm horizontally and 2 cm vertically.

Raman mapping systems are generally confocal, i.e. only the signal coming from the near object focal plane is redirected to the spectrometer. This is done by placing a pin hole in the image focal plane of the microscope. The volume used for the analysis is then reduced and the in-plane resolution is slightly increased, depending on the size of the pin hole, the objective and the laser wavelength. The main interest of the confocality is to permit 3D imaging using a stacking process by acquiring Raman maps at different depths. It is important to note that the

depth of analysis depends on the refractive index of the material; there is a difference between the apparent depth, corresponding to the distance with respect to the sample surface, and the true depth of analysis (**Figure 2**).

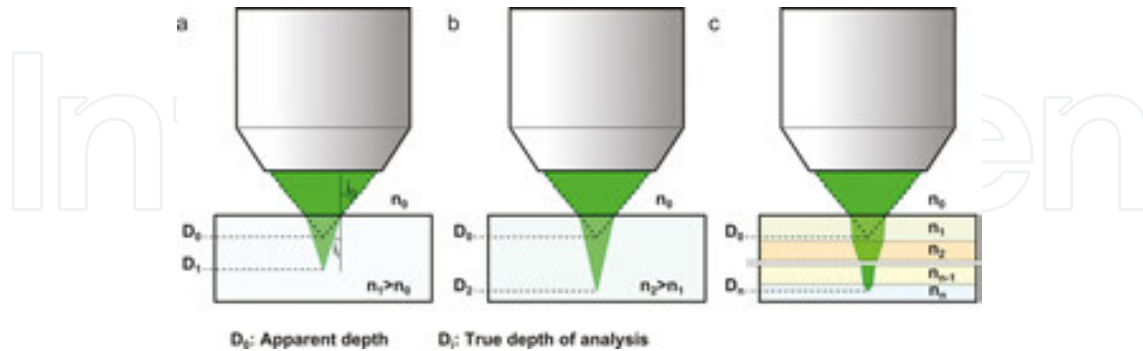


**Figure 2.** Apparent depth  $D_0$  versus true depth  $D_i$  of analysis in optical microscopy when analysing (a) a material with a refractive index equal to  $n_1$ , (b) a material with a refractive index equal to  $n_2$  with  $n_2 > n_1$  and (c) when analysing across  $n$  different materials of refractive index  $n_i$  and thickness  $e_i$ .

The ratio between the true depth  $D_i$  and the apparent depth  $D_0$  is given by the following equation:

$$\frac{D_i}{D_0} = \frac{\tan i_0}{\tan i_1} \quad (1)$$

where  $i_0$  and  $i_1$  are the maximal angle with respect to the optical axis in the observation medium (e.g. air, water or oil) and in the analysed material, respectively (see **Figure 2a**). The famous Snell-Descartes law and the definition of the numerical aperture NA give:

$$NA = n_0 \cdot \sin i_0 = n_i \cdot \sin i_i \quad (2)$$

where  $n_0$  and  $n_i$  are the refractive index of the observation medium and of the analysed material, respectively. Using Eq. (2), and noting that:

$$\tan(\arcsin x) = \frac{x}{\sqrt{1-x^2}} \quad (3)$$

Eq. (1) finally writes:

$$\frac{D_i}{D_0} = \sqrt{\frac{n_i^2 - NA^2}{n_0^2 - NA^2}} \quad (4)$$

This ratio is thus all the more important when the difference in refractive index is high (see **Figure 2b**). For example, when analysing quartz ( $n_{\text{qz}} = 1.55$ ) in air ( $n_{\text{air}} = 1$ ) with an objective having a numerical aperture of  $NA = 0.9$ , the true depth of analysis is  $\sim 2.9$  times deeper than the apparent depth corresponding to the mechanical vertical displacement.

In the case where several phases are crossed by the laser (see **Figure 2c**), Eq. (4) can be generalised into:

$$\frac{D_n}{D_0} = \sum_{i=1}^n e_i \sqrt{\frac{n_i^2 - NA^2}{n_0^2 - NA^2}} \quad (5)$$

where  $e_i$  is the thickness of the phase  $i$ . For 2D maps, the depth of the measurement and the volume analysed are thus different for each phase, and for 3D Raman maps, the volume and the depth of the different phases are associated with different scales in the raw data.

### 2.3. Raman mapping

As explained above, Raman mapping consists of scanning the sample with the laser beam while acquiring spectra. The scanned area is then divided into a pixel-assigned array of spectral elements, sometimes called “spexels” [8], as shown in **Figure 3a**.

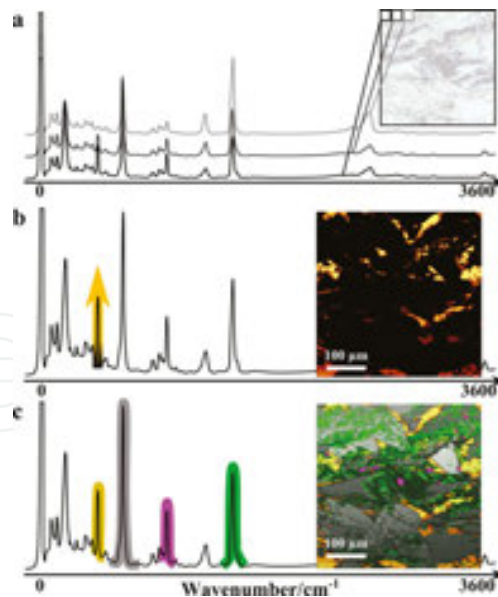


**Figure 3.** (a) Principles of Raman mapping illustrated using a polished thin section of a metachert from the 3.8 billion years old Isua Greenstone belt, Greenland. The scanned area of the sample is divided into small squares, or spexels, each associated with a Raman spectrum. (b) Raman map of the concentration of quartz in the sample, as identified by the intensity of the main peak at  $465 \text{ cm}^{-1}$ . (c) Raman map of the composition of the sample obtained by attributing a colour to the main spectral peak of each mineral (yellow for quartz, grey for cumingtonite, pink for apatite and green for graphite). Scan size:  $500 \times 500 \text{ }\mu\text{m}^2$ .



Historically, the first Raman maps were constructed manually by making a map point by point. The sample was then not scanned continuously but was immobile beneath the laser beam during the acquisition of each spectrum (Figure 4). These first maps were interesting for the study of homogeneity in materials, but, because of the limited number of spectra associated with this time-consuming method, imaging was not very efficient. With the recent development in fine positioning systems and synchronisation between the positioning system and the CCD detector, automated scanning is now available. This automation allows high resolution mapping point by point as well as by continuous scanning.

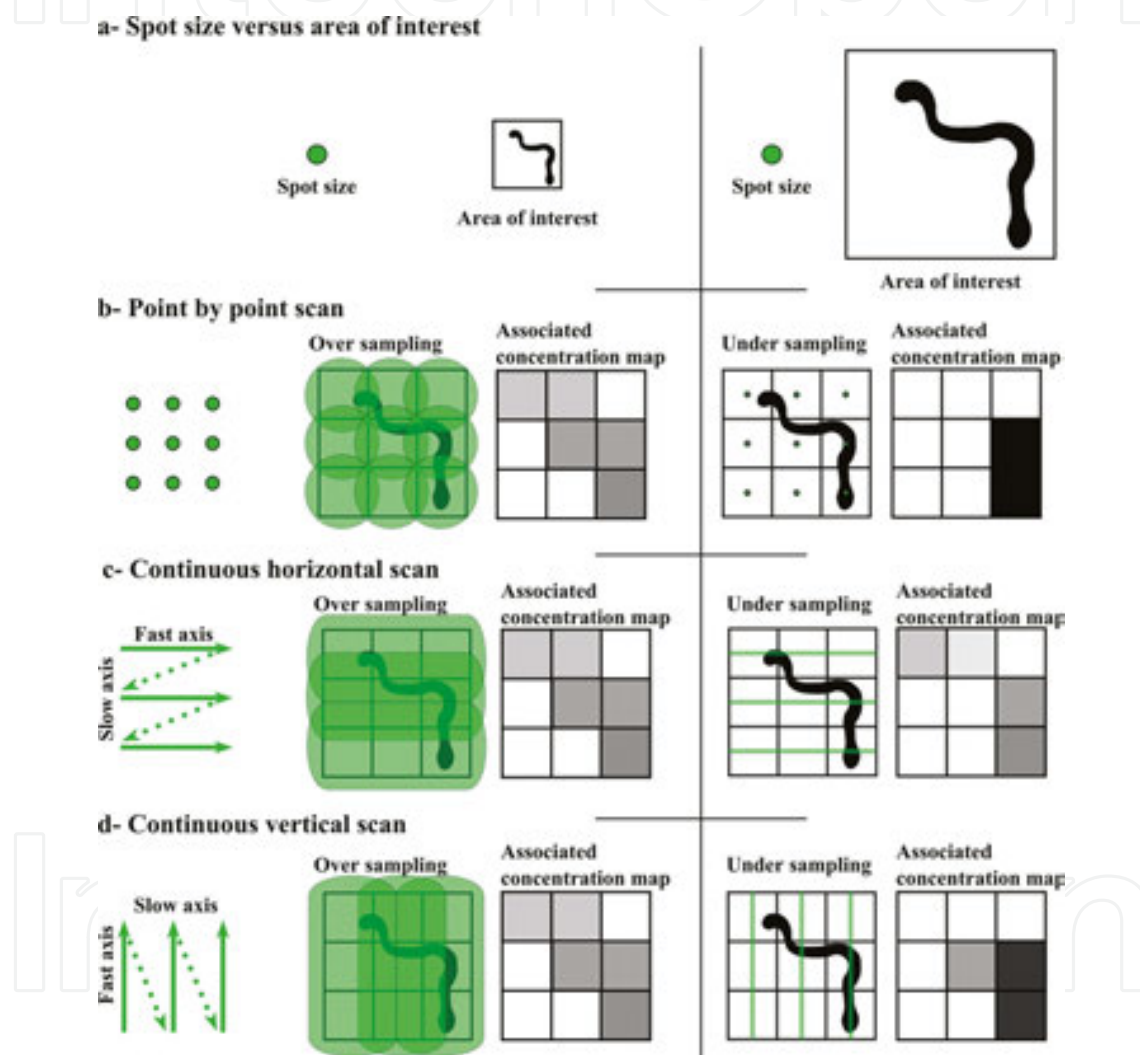


**Figure 4.** Principle of Raman mapping. (a) Laser spot size versus area of interest and different ways of scanning, (b) point by point, (c) continuously and horizontally and (d) continuously and vertically. The spectrum associated to each pixel corresponds to the average spectrum of the different associated phases. The concentration map is thus darker where the vermicular structure is analysed. If the spot size is larger than the pixel size (left row), there is oversampling, and the associated maps are the same whatever the method used. However, if the laser spot size is small in comparison with the pixel size (right row), there is undersampling and the associated maps depend on the type of the scan.

In all scanning methods of imaging (e.g. Raman mapping as well as atomic force microscopy, scanning electron microscopy, etc.), the lines are accumulated one by one and the spatial

resolution is fixed by the ratio of the width and height of the scanned area over the number of lines and rows, respectively. Then, for a square scan, the time needed to go down a row is very long compared to the time needed to go along a line (for a horizontal scan). The axis parallel to the lines is thus called the fast axis, and the axis perpendicular to the lines is called the slow axis (see **Figure 4**). This notion must be kept in mind while scanning a small area where thermal or mechanical drift may induce deformation in the images (shearing) and/or a loss of focus with the time. During Raman mapping, the spectra are generally accumulated continuously during the scan. The spectrum associated with each point corresponds thus to the average spectrum acquired over a line whose length is fixed by the spatial resolution but whose thickness is equal to the laser spot size. If the spot size is higher than the resolution, the associated map is then under-sampled since not all the area are scanned; a scan obtained over the same area rotated by 90° would give a different result (**Figure 4**). To avoid this effect, the chosen resolution must be at least equal to the spot size. On the other hand, the Rayleigh criterion implies that the resolution cannot be physically higher than half of the spot size as given by the Airy disk equation:

$$S = 1.22 \frac{\lambda}{NA} \quad (6)$$

where  $\lambda$  is the laser wavelength,  $S$  is the laser spot diameter, and  $NA$  is the numerical aperture of the objective. Using a green laser ( $\lambda = 532$  nm) and the 100× objective (with a numerical aperture of 0.9), the spot size is thus  $S \sim 720$  nm in diameter and the maximal physical resolution is thus  $\sim 360$  nm/pixel. Using a confocal system, this resolution can be slightly decreased by  $\sim 10\%$  [6]. However, even if using a higher resolution does not give more information, over-sampling could provide a better contrast.

In conclusion, continuous scanning is generally the best choice for imaging due to its rapidity, but point-by-point mapping may be useful when the sample contains fluorescent phases that may drown out the Raman signal of the other phases in the average spectra acquired with the continuous scan method.

### 3. Data processing

We have chosen a number of different rocks and minerals to illustrate methods of data processing for improving image quality and for obtaining specific information. Measurements were made mainly on polished thin sections as well as on polished rock surfaces.

#### 3.1. Classical maps

Raman scans are mostly used to map the composition of a sample over a particular area. The interest of mapping with respect to single spectrum analysis is that it is possible to observe the association and spatial distribution of different phases (see **Figure 5**). These kinds of images



are obtained by selecting a peak in the spectrum of each phase and by plotting its intensity in order to obtain an image of its concentration (**Figures 3b** and **5b**), or by associating a colour to a given peak in order to obtain an image in which each phase is represented by a colour (**Figures 3c** and **5d**). However, the quality of the images can be improved by more complex data processing. The use of the peak area instead of the peak intensity leads to slightly better contrast, in particular if the peak is wide (**Figure 5c**). A second step involves extracting the spectrum of each phase and using a correlation process with the global data set to dissociate phases when there is partial overlap of their peaks (**Figure 5d–f**). Calculations can be applied to the data set, such as derivatives to eliminate the background or to use the square or the cube of the data set to increase the signal/noise ratio. Finally, more advanced tools can be used, such as principal component analysis, to improve the detection of different phases [9].

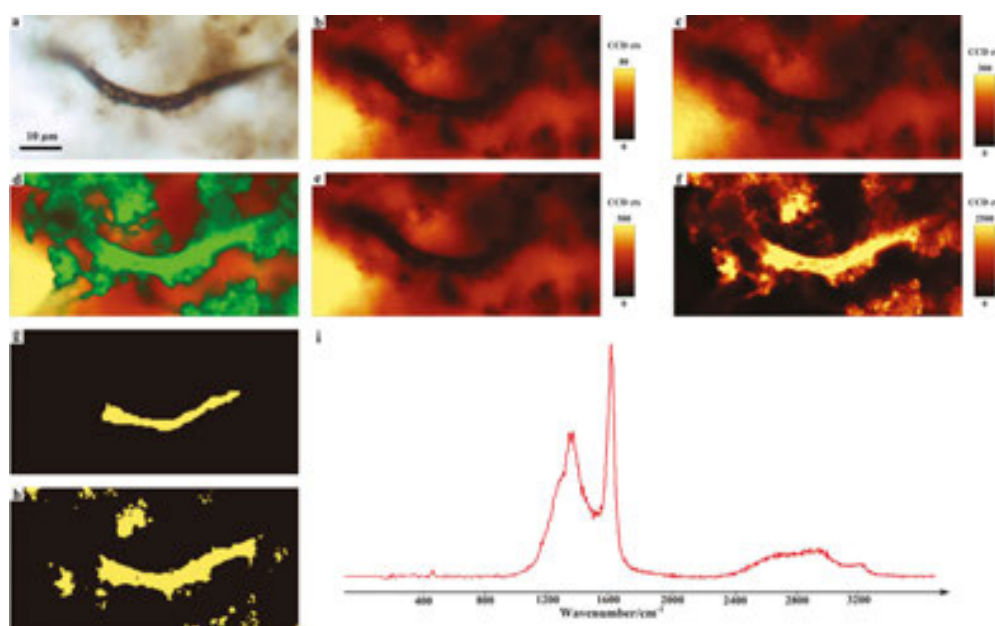


**Figure 5.** Raman mapping of silicified microorganisms from the Gunflint formation and average spectrum of carbonaceous matter. (a) Optical microscopy image in transmitted light. Associated Raman images of quartz obtained (b) using the intensity of the main peak of quartz at  $465\text{ cm}^{-1}$  and (c) the area of the same peak. (d) Raman compositional map with quartz in orange and carbonaceous matter in green corresponding to the superimposition of the Raman images obtained using the full spectrum correlation of (e) quartz and (f) carbonaceous matter. Boolean masks (0 in black and 1 in yellow) can be obtained by directly drawing on the image (g) or by using a mathematical threshold filter (h) in order to obtain a high signal/noise ratio average spectrum of the fossilised filament (i).

Mapping also permits by obtaining high quality spectra of a phase. Indeed, it is possible to create a mask (i.e. Boolean image) by directly drawing on an image (**Figure 5g**) or by using thresholds (**Figure 5f**) to select the areas of interest, to multiply it to the data set in order to select only the associated spectra, and finally to average these spectra to obtain the corresponding average spectrum (**Figure 5i**). Different masks can be applied to the same data set. For example, it is possible to use a mask corresponding to the area where the signal of the phase is the highest and a second one corresponding to the areas where the background level is the lowest. The average spectrum thus obtained can be more representative than that

obtained in only one point. Of course, the map can also be used to locate the area where the signal is highest before acquiring a single spot spectrum.

### 3.2. Detection and identification of small phases

Although the spatial resolution of Raman spectroscopy is the same as that of optical microscopy, each pixel of an image is not just a colour but corresponds to a spectrum. Raman spectroscopy may thus permit identification of very small grains that are difficult to identify using classical optical microscopy (e.g. the pyrite grain shown by the black arrow in **Figure 6c** or the grain of SiC in **Figure 9d**). A mineral phase may also be invisible in optical microscopy, and Raman mapping is then the only way to detect it, as shown in **Figure 6**. Finally, at larger scales, mapping can be a good means to localise phases present in minor or trace amounts in a sample.

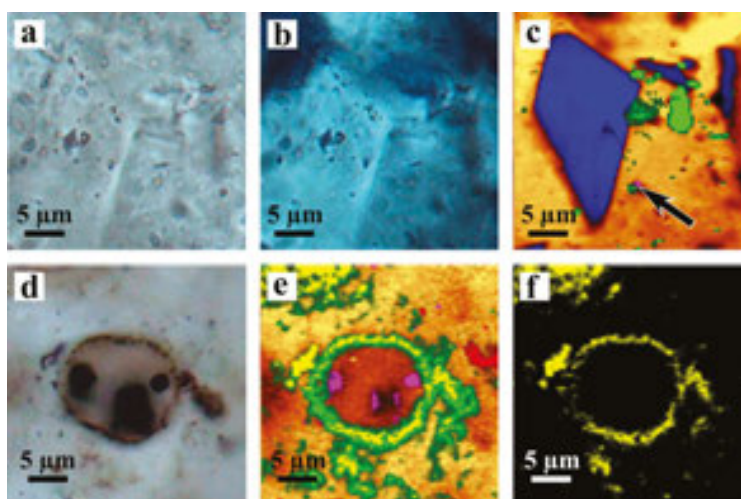


**Figure 6.** Optical and associated Raman maps of (a–c) a polished thin section of a hydrothermal vein from the quarry of Neuvial, Mazerier, Allier, France and (d–f) a thin section of the ~800 My-old Draken Formation, Svalbard (see [10] for more information). The Raman map (c) shows the presence of carbonaceous matter (green), orthoclase (blue) and a pyrite grain (pink and black arrow) in the quartz matrix (orange). The carbonaceous matter and the pyrite grain were invisible in the optical microscopy image (a), and the orthoclase was too small to be identified by polarised optical microscopy (b). The optical image (d) shows a fossil planktonic microorganism. The presence of opal (in yellow) and anatase (in red) is highlighted in the composition (e) and opal (f) Raman maps, whereas they are invisible in optical microscopy. The quartz matrix is in orange in (e). Image size  $30 \times 30 \mu\text{m}^2$ .

### 3.3. Identification of spectrally close phases

Not only is the spatial resolution better than mapping but also the spectral resolution. Indeed, due to the high number of spectra accumulated for each image, very small spectral changes can be statistically detected. **Figure 7** shows the position of the centre of mass of the main peak of a quartz spectrum during analysis of crushed samples of various grain sizes (see Ref. [1] for more information). Although the resolution of the Raman spectrometer is  $\sim 1 \text{ cm}^{-1}$ , the image highlights peak shifts lower than  $0.5 \text{ cm}^{-1}$ . Such small variations would not be identifiable using single spectrum analysis, while they are statistically obvious in this image.

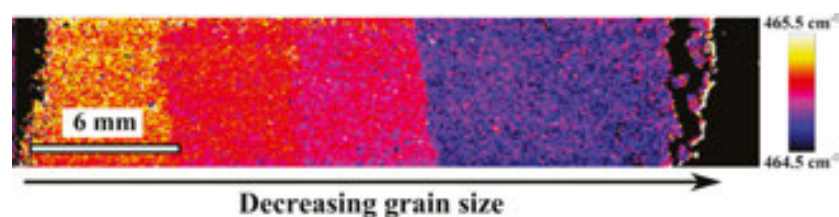


**Figure 7.** Raman analysis of quartz powders of four different grain sizes (decreasing grain size from left to right) showing the shift of the main peak at  $\sim 465\text{ cm}^{-1}$  towards the lower values with the decreasing grain size (see Ref. [1] for more information).

A similar approach can be helpful for mineralogy because it is often difficult to distinguish minerals having relatively similar Raman spectra, for example, carbonates [11]. However, by using peak position and the full width of the peaks at half maximum (FWHM) or the background level, it is possible to distinguish and identify different phases in the images. **Figure 8** shows different Raman images obtained from the same data set of carbonate deposits in a vesicle in basalt from Svalbard (see Refs. [12] and [13] for more information). The different carbonate phases can be distinguished because of the variation in the ratio Mg/Ca during deposition, resulting in phases ranging from dolomite to magnesite.

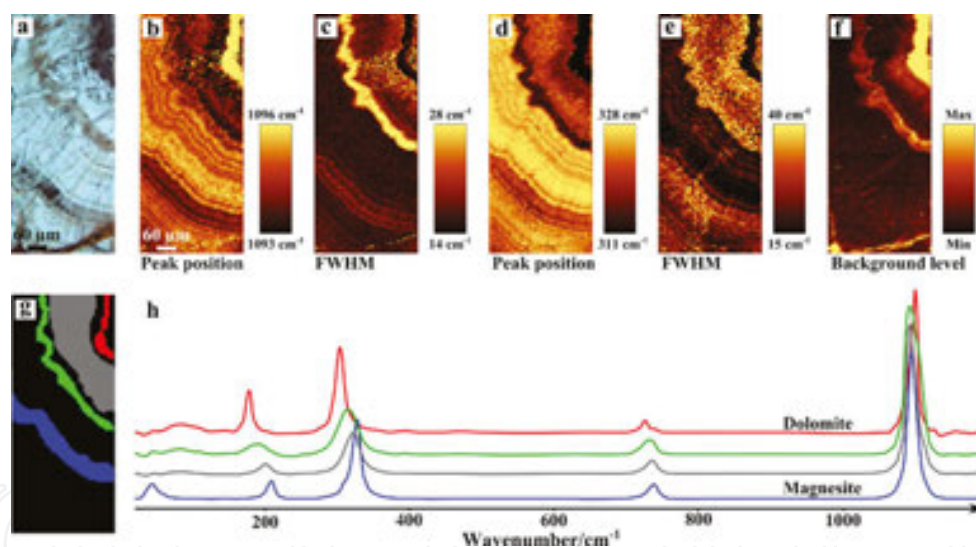


**Figure 8.** (a) Optical image and Raman maps of (b) the position, (c) the FWHM of the main peak position around  $1000\text{ cm}^{-1}$ , (d) and (e) of the second carbonate peak around  $320\text{ cm}^{-1}$  and (f) the background level illustrating different phases in carbonate deposited in a vesicle formed in basalt from Svalbard (see Ref. [13] for more information). The corresponding areas can be selected (g) in order to obtain the associated average spectra (h).

### 3.4. Exotic uses

As noted above, the collected signal depends on different parameters that can be used to make images. More complex maps can thus be obtained by applying different calculations to the images; for instance, the ratio of peak intensity can distinguish changes in crystal orientation, as shown in **Figure 9**. The image of background intensity is also a particularly interesting



example. We have seen above that it can be used to make masks, but it can also be used to show variations in composition or to distinguish relatively similar phases (**Figure 8**). The Raman signal can also be modified by defects in the sample, such as cracks or fluid inclusions, as shown in **Figure 9**. Finally, the signal is also associated with fluorescence and could thus give some information about the trace element composition of a mineral.

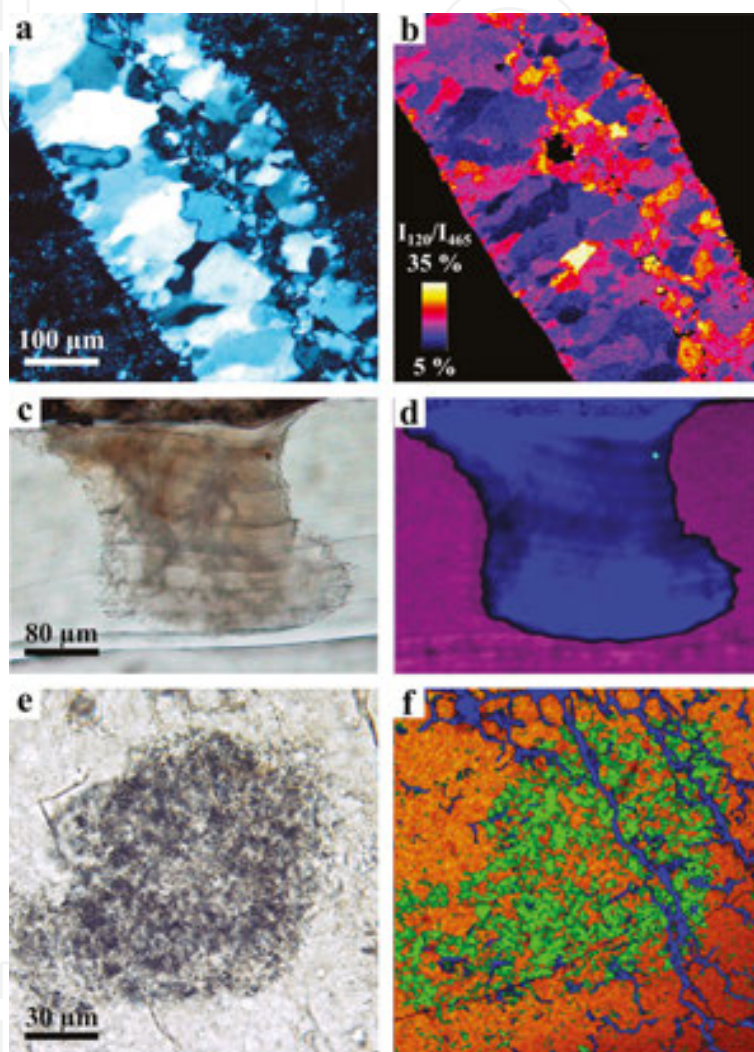


**Figure 9.** (a) Optical image in polarised/analysed transmitted light microscopy and (b) associated compositional Raman map of a polished thin section of hydrothermal quartz vein (Barberton, South Africa). The image of the intensity ratio of the peak located at  $465\text{ cm}^{-1}$  over the peak located at  $120\text{ cm}^{-1}$  permits highlighting differences in crystalline orientation. (c) Optical image and (d) associated compositional Raman map of a polished thin section of a pearl showing aragonite in purple and vaterite in dark blue. The background intensity image is used to show the vaterite (see Ref. [14] for more information). A small grain of SiC, coming from the polishing process, is also detected (in light blue in d). (e) Optical image and (f) associated compositional Raman map of a chert sample having undergone atmospheric entry (analogue meteorite, see Ref. [15] for more information). The quartz is in orange and the carbonaceous matter in green. The background intensity is displayed in dark blue and highlights cracks in the sample due to stresses related to atmospheric entry.

To conclude, various processing methods applied to Raman mapping data set can highlight particular properties of the mineral phases in a scanned sample. Further examples of such

processing include making several scans of the same area using different environmental parameters (different laser wavelengths, external stress, temperature, etc.).

### 3.5. Statistical treatment

In all the above maps, the increase in information due to the statistics of a great number of spectra is implemented visually by plotting the appropriate classic spectral parameters. When the components of the sample are unknown, the reference spectra are not available, and the spectral sources are not well identified from spectrum to spectrum, or to extract very fine spectral modification of a single compound, mathematical treatment based on the statistical structure of the hyperspectral data can be implemented. Nowadays, numerous mathematical treatments exist and are tested by spectroscopists in various kinds of applications [9, 16, 17]. As an illustration, **Figure 10** shows the principal component analysis extraction of spectral sources of interest in the Raman mapping of a uranium dioxide ceramic and the corresponding

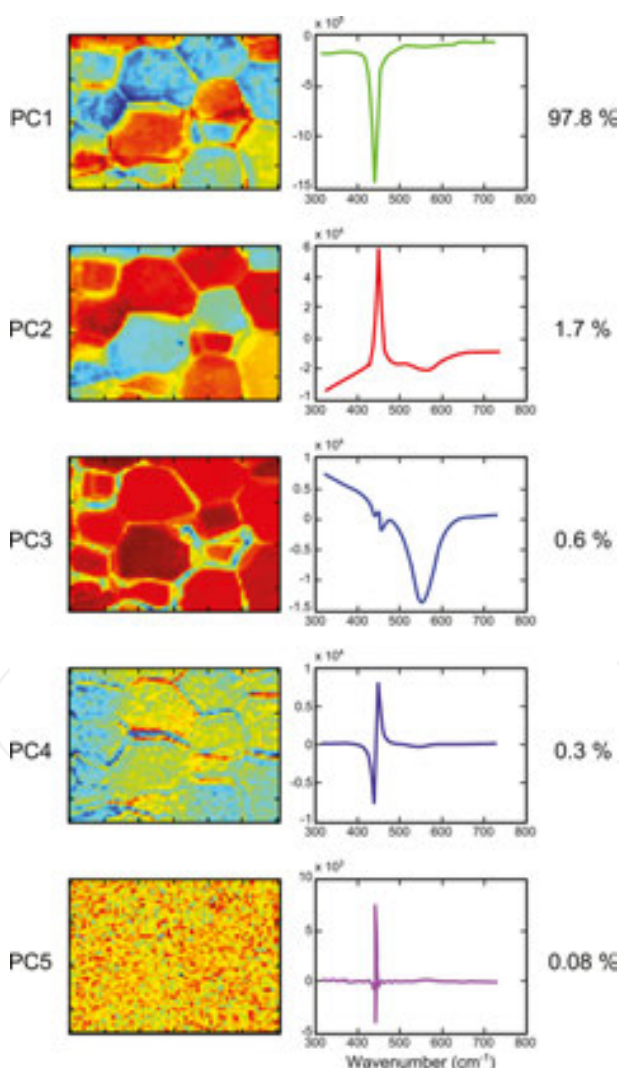


**Figure 10.** Principal component analysis of a Raman mapping of a uranium dioxide ceramic. At right, the spectral sources with their percentages and at left, the corresponding maps [9].

map [9]. The percentages to the right are the percentage of data variance coming from the corresponding spectral source. The maps show that only the first four sources have any significance, the fifth being only noise. Analysis of the information given by the spectral sources is complex. An initial analysis demonstrates the fact that different types of maps highlight either the grains or the grain borders in the ceramic (see Ref. [9] for more details).

## 4. Gallery

**Figure 11** shows various examples of Raman maps made on polished thin sections of various rocks. As described below, the mineralogical determination and the interpretation of minerals in their context are greatly facilitated by Raman mapping.

### 4.1. Sedimentary samples

The sample in **Figure 11a** is a sandstone with an oxide matrix coming from the Hettangien formation (203.6–199.6 My), Chéniers France (see Ref. [18] for more information). This formation was occasionally exploited for iron and manganese since the Iron Age and also contains barite mineralisation. The grains consist of quartz and plagioclase (**Figure 11a1**). The different phases of iron oxide crystallisation in the holes of the rock, where hematite is altered to goethite, are highlighted by Raman mapping (**Figure 11a2**). These minerals are difficult to distinguish in transmitted light by optical microscopy. A small grain of barite is also visible in the Raman map.

### 4.2. Magmatic sample

Magmatic rocks are in most cases relatively easy to study using optical microscopy (the crystals are large and euhedral). However, Raman mapping can reveal small variations in mineralogical phases or crystal orientation. **Figure 11b1** shows an optical view of a granite from Autun, Saône-et-Loire, France (see Ref. [19] for more information). This rock is composed of large grains of quartz and labradorite associated with biotite, phlogopite, plagioclase and accessory minerals (titanite, apatite, rutile and brookite; **Figure 11b2**).

### 4.3. Volcanic samples

The sample shown in **Figure 11c** is a basalt from El Teide volcano, Tenerife, Spain. Basaltic rocks containing glass and microlitic crystals tend to be rather opaque in thin section, and identification of the individual minerals using optical microscopy is difficult, as shown in **Figure 11c1**. On the other hand, Raman mapping reveals easily all the microlitic paragenesis (labradorite, augite, analcime, apatite, anatase and hematite; **Figure 11c2**). Analcime occurs in vesicles and is a secondary mineral in this basalt. **Figure 11c3** shows the crystalline orientation of the plagioclases phases with polysynthetic twinning obtained from the intensity ratio of the spectral peaks at 195 and 514  $\text{cm}^{-1}$ . With this type of sample, a statistic treatment of the image could provide information on the orientation of the minerals and, consequently, lava flow direction.



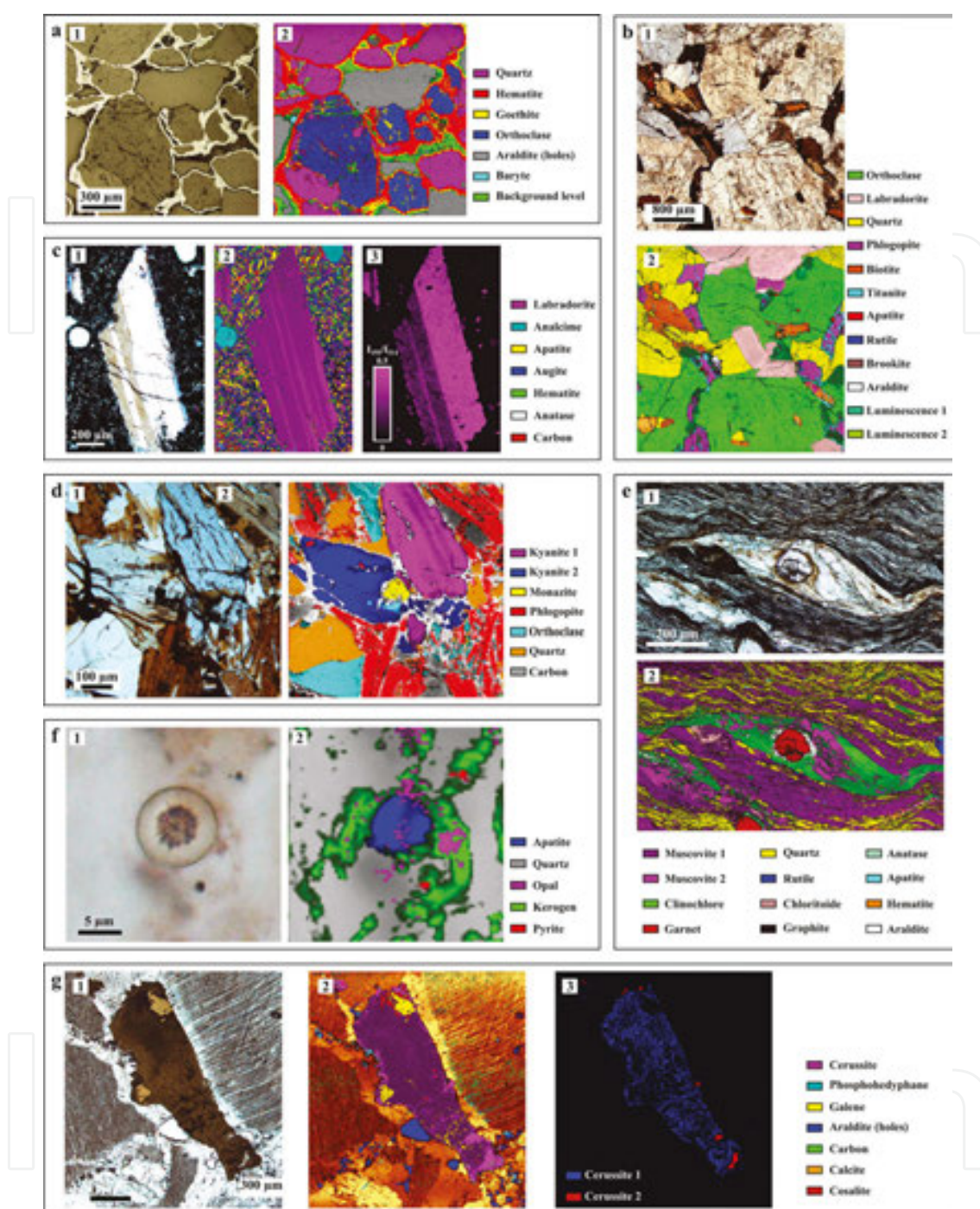


**Figure 11.** Image gallery made on polished thin sections of different samples. (a) Sandstone from the Chéniers mine, Sacierges-Saint-Martin, Indre, France, (a1) optical view in reflected light, (a2) Raman map. (b) Granite from Autun, Saône-et-Loire, France (b1) optical view of the rock, (b2) Raman map. (c) Basalt from El Teide volcano, Tenerife, Spain (c1) optical view in transmitted light, (c2) Raman map and (c3) detail of the orientation in a plagioclase crystal obtained from the intensity ratio of the spectral peaks at 195 and 514  $\text{cm}^{-1}$ . (d) Garnet-kyanite granulite xenoliths in gneiss from La ferme des Saugères, Allier, France (d1) optical view in transmitted light, (d2) Raman map. (e) Highly deformed micaschist from the Sierra Alhamilla, Almería, Spain (e1) optical view of a pressure shadow around a garnet in transmitted light, (e2) Raman map. (f) Microfossil from the Draken formation, Svalbard (f1) optical view in transmitted light, (f2) Raman map. (g) "Calamine" (Zn ore rocks) sample from Beni Tajite mine, Haut Atlas, Morocco (g1) optical view, (g2) Raman map and (g3) detail of two generations of cerussite.

#### 4.4. Metamorphic samples

Metamorphic rocks are characterised by very different mineral paragenesis, which can be difficult to identify in optical microscopy but easily resolvable using Raman mapping.

The sample in **Figure 11d** is a garnet-kyanite granulite from the gneissic upper unit (USG), La Ferme des Saugères in the Sioule metamorphic series, Allier, France (see Refs. [20] and [21] for more information). This rock is composed of quartz and granoblastic orthoclase that are readily visible in the Raman map (**Figure 11d2**). A particularity of this sample is that it presents a retromorphosed facies associated with the destabilisation of the garnet and kyanite to phlogopite. Identification of the  $\text{Al}_2\text{SiO}_5$  polymorphs (andalousite, sillimanite and kyanite) by optical microscopy is difficult but not with Raman mapping. The information thus obtained could be helpful for establishing the conditions of formation of the rock (e.g. in a P-T-t diagram). **Figure 11d2** is a Raman map based on peak parameters that have been modified by changes in the crystal orientation of kyanite. Note that carbon is present because the sample was coated for analysis by scanning electron microscopy and electron microprobe.

The second metamorphic sample is a highly deformed micaschist from the Sierra Alhamilla, Almería, Spain (see Ref. [22] for more information). **Figure 11e1** is an optical micrograph demonstrating the high degree of deformation of the rock, making identification of the individual phases difficult. Raman mapping, on the other hand, reveals that the rock contains chloritoid relics as well as various accessory minerals such as rutile, anatase, apatite, graphite and hematite in a small alteration vein. A pressure shadow filled by clinochlore and a new generation of muscovite can be observed. With its ability to distinguish structural changes in individual minerals, Raman mapping also highlights the direction of deformation, as indicated by the quartz and muscovite crystals (**Figure 11e2**).

#### 4.5. Application for micropaleontology

**Figure 11f** is a dolomitised conglomerate from the Draken Formation (–800 to –700 My), Svalbard. This conglomerate includes cherty lenses rich in microbial mat/planktonic microfossil assemblages (**Figure 11f1**) [23]. Two colourless phases that are not distinguishable in optical microscopy are revealed by Raman mapping to be opal and hydroxyapatite (**Figure 11f2**) (see Ref. [10] for more information). Some small spots of pyrite are also observed.

#### 4.6. Application for metallogeny

Mineral identification in metallogeny is very important for understanding the mineralisation process. **Figure 11g1** shows calamine deposit from the Beni Tajite mine, Haut Atlas, Morocco, developed in a karstic area (see Ref. [24] for more information). The Raman map in **Figure 11g2, 3** shows the presence of cerussite formed by the alteration of galena. The cerussite has a botryoidal banded texture and forms a crust shielding the galena from oxidation. Some cerussite recrystallised during evolution of the karst, resulting in two generations of the mineral, each characterised by very specific textures that are invisible to optical or electronic microscopy but are readily visible in Raman mapping. Other minerals, such as calcite, cosalite

(a Pb-Bi-sulphur) and phosphohedyphane (a Pb-phosphate), can also be identified by Raman mapping.

## 5. Conclusion

Raman mapping is a powerful technique for mineralogy and petrography. The small spatial resolution of the laser beam allows detection and identification of very small mineral phases that are impossible to identify by optical microscopy. The spectral resolution is also considerably improved by the rapid acquisition of several thousands of spectra. Finally, various data processing methods can be used to characterise particular structural or compositional properties of individual crystalline phases, thus vastly improving analytical possibilities. In the near future, mapping is likely to become the standard procedure for Raman analysis.

## Acknowledgements

We acknowledge Olga A. Maslova for the mapping and analysis of UO<sub>2</sub> ceramics. R. Augier, F. Choulet, D. DoCouto and F. Rull for the samples from Sierra Alhamilla, Morocco and Autun, la Sioule and Tenerife, respectively. We also acknowledge P. Bost for his help in sampling at Chéniers.

## Author details

Frédéric Foucher<sup>1\*</sup>, Guillaume Guimbretière<sup>2</sup>, Nicolas Bost<sup>2</sup> and Frances Westall<sup>1</sup>

\*Address all correspondence to: frederic.foucher@cnrs-orleans.fr

1 CNRS, Centre de Biophysique Moléculaire, France

2 CNRS, Conditions Extrêmes: Matériaux, Hautes Températures et Irradiation, France

## References

- [1] Foucher F, Lopez-Reyes G, Bost N, Rull Pérez F, Russmann P, Westall F. Effect of grain size distribution on Raman analyses and the consequences for in situ planetary missions. *Journal of Raman Spectroscopy*. 2013;44:916–925.
- [2] Guimbretière G, Desgranges L, Canizares A, Carlot G, Caraballo R, Jegou C, Duval F, Raimboux N, Ammar M-R, Simon P. Determination of in depth damaged profile by



micro-Raman line mapping in a pre-cut irradiated UO<sub>2</sub>. *Applied Physics Letters*. 2012;100:251914.

- [3] Guimbretière G, Canizarès A, Raimboux N, Joseph J, Desgardin P, Desgranges L, Jegou C, Simon P. High temperature Raman study of UO<sub>2</sub>: A possible tool for in situ estimation of irradiation-induced heating. *Journal of Raman Spectroscopy*. 2015;46:418–420.
- [4] Gries T, Vandenbulcke L, Simon P, Canizares A. Anisotropic biaxial stresses in diamond films by polarized Raman spectroscopy of cubic polycrystals. *Journal of Applied Physics*. 2008;104:023524.
- [5] Poilblanc R, Crasnier F. Spectroscopies infrarouge et Raman. In: Bornarel J, editor. *Collection Grenoble Sciences, Les Ulis, France: Grenoble, EDP Sciences; 2006. 674 p.*
- [6] Dieing T, Hollricher O, Toporski J, editors. *Confocal Raman Microscopy. Springer Series in Optical Sciences, 156th ed. Berlin, Germany: Springer; 2010. 289 p.*
- [7] Dubessy J, Caumon M-C, Rull Pérez F, editors. *Raman Spectroscopy Applied to Earth Sciences and Cultural Heritage. EMU Notes in Mineralogy, 12th ed. Twickenham, United Kingdom: The Mineralogical Society of Great Britain and Ireland; 2012. 504 p.*
- [8] Schopf JW, Kudryavtsev AB, Agresti DG, Czaja AD, Wdowiak TJ. Raman imagery: A new approach to assess the geochemical maturity and biogenicity of permineralized precambrian fossils. *Astrobiology*. 2005;5(3):333–371.
- [9] Maslova OA. *Caractérisation de matériaux heterogenes par spectroscopie Raman [thesis]. University of Orléans, France; 2014.*
- [10] Foucher F, Westall F. Raman imaging of metastable opal in carbonaceous microfossils of the 700–800 Ma old Draken formation. *Astrobiology*. 2013;13(1):57–67.
- [11] Rividi N, van Zuilen M, Philippot P, Ménez B, Godard G, Poidatz E. Calibration of carbonate composition using micro-Raman analysis: Application to planetary surface exploration. *Astrobiology*. 2010;10(3):293–309.
- [12] Treiman AH, Amundsen HEF, Blake DF, Bunch T. Hydrothermal origin for carbonate globules in Martina meteorite ALH84001: Terrestrial analogue from Spitsbergen (Norway). *Earth and Planetary Science Letters*. 2002;204:323–332.
- [13] Bost N, Westall F, Ramboz C, Foucher F, Pullan D, Meunier A, Petit S, Fleischer I, Klingelhöfer G, Vago J. Missions to Mars: Characterisation of Mars analogue rocks for the International Space Analogue Rockstore (ISAR). *Planetary and Space Science*. 2013;82–83:113–127.
- [14] Bourrat X, Foucher F, Guegan R, Feng Q, Stemfle P, Chateigner D, Westall F. AFM-Raman coupling to study mesocrystal polymorphism in nacre. In: *GeoRaman Xth. France: Nancy; 2012. p. 27.*
- [15] Foucher F, Westall F, Brandstätter F, Demets R, Parnell J, Cockell CS, Edwards HGM, Bény J-M, Brack A. Testing the survival of microfossils in artificial martian sedimentary

meteorites during entry into Earth's atmosphere: The STONE 6 experiment. *Icarus*. 2010;207:616–630.

- [16] Vajna B, Patyi G, Nagy Z, Bodis A, Farkas A, Marosi G. Comparison of chemometric methods in the analysis of pharmaceuticals with hyperspectral Raman imaging. *Journal of Raman Spectroscopy*. 2011;42:1977–1986.
- [17] Gendrin C, Roggo Y, Collet C. Pharmaceutical applications of vibrational chemical imaging and chemometrics: A review. *Journal of Pharmaceutical and Biomedical Analysis*. 2008;48:533–553.
- [18] Vincienne H. Rapport géologique sur le gisement de fer du bassin de Chaillac (Indre). Chambre de commerce et d'industrie de l'Indre, France 1948; p. 26.
- [19] Choulet F, Faure M, Fabbri O, Monié P. Relationships between magmatism and extension along the Autun-La Serre fault system in the Variscan Belt of the eastern French Massif Central. *International Journal of Earth Science (GeolRundsch)*. 2012;101:393–413.
- [20] Ravier J, Chenevoy M. Présence de formations granulitiques jalonnant un linéament crustal dans la série cristallophylienne de la Sioule (Massif Central Français). *Compte Rendu de l'Académie des Sciences de Paris*. 1979;288(II):1703–1706.
- [21] DoCouto D. Signification géologique des datations chimiques sur monazite. Application à la série polymétamorphique de la Sioule (Nord du Massif Central) [Master 2 thesis]. Université d'Orléans, France ; 2009.
- [22] Augier R, Agard P, Monié P, Jolivet L, Robin C, Booth-Rea G. Exhumation, doming and slab retreat in the Betic Cordillera (SE Spain): In situ  $40\text{Ar}/39\text{Ar}$  ages and P–T–d–t paths for the Nevado-Filabride complex. *Journal of Metamorphic Geology*. 2005;23:357–381.
- [23] Knoll AH, Fairchild IJ, Swett K. Calcified microbes in Neoproterozoic carbonates: Implications for our understanding of the Proterozoic/Cambrian transition. *Palaeos*. 1993;8(6):512–525.
- [24] Charles N, Barbanson L, Sizaret S, Ennaciri A, Branquet Y, Badra L, Chen Y, El Hassani L, Guillou-Frottier L. Les gisements à ZN non-sulfurés du Haut-Atlas marocain. Ressources minérales: la vision du mineur. In: Ecole thématique CNRS/INSU/MINES. Paris: Tech; 2012.